Jupiter's Hotspots as observed by JIRAM-Juno: limb darkening in thermal infrared

D. Grassi [ORCID],[1]★ A. Mura [ORCID],[1] A. Adriani,[1] G. Sindoni,[2] S. K. Atreya,[3] L. N. Fletcher [ORCID],[4] G. S. Orton,[5] C. Plainaki,[2] F. Tosi [ORCID],[1] F. Biagiotti,[1,6] A. Olivieri,[2] C. Castagnoli,[1,7,8] E. D'Aversa,[1] A. Migliorini [ORCID],[1] A. Moirano,[1,6] R. Noschese,[1] G. Piccioni,[1] R. Sordini[1] and S. Bolton[9]

[1]*Istituto di Astrofisica e Planetologia Spaziali, Istituto Nazionale di Astrofisica, Rome, 00133, Italy,*
[2]*Direzione Scienza e Innovazione, Agenzia Spaziale Italiana, Rome, 00133, Italy*
[3]*Department of Climate and Space Sciences and Engineering, University of Michigan, Ann Arbor, MI, 48109, USA*
[4]*School of Physics and Astronomy, Univerisity of Leicester, Leicester, LE1 7RH, UK*
[5]*Jet Propulsion Laboratory, California Institute of Technology, Pasadena, CA, 91011, USA*
[6]*Dipartimento di Fisica, Università degli Studi di Roma 'Sapienza', Roma, 00185, Italy*
[7]*Dipartimento di Fisica, Università degli Studi di Roma 'Tor Vergata', Roma, 00133, Italy*
[8]*Istituto di Scienze dell'Atmosfera e del Clima, Consiglio Nazionale delle Ricerche, Bologna, 40129, Italy*
[9]*Southwest Research Institute, San Antonio, TX, 78238, USA*

ABSTRACT

The Jupiter InfraRed Auroral Mapper (JIRAM) instrument onboard the Juno spacecraft performed repeated observations of Jupiter's North Equatorial Belt (NEB) around the time of 12th Juno pericenter passage on 2018 April 1. The data consist of thermal infrared images and show, among other atmospheric features, two bright Hotspots on the boundary between the NEB and the Equatorial Zone. Night-time images of the same areas at different emission angles were used to constrain the trend of the limb-darkening function. Comparison with simulated observations, computed for different emission angles, total opacities, single scattering albedo ω_0, and asymmetry parameter g suggests that $\omega_0 \sim 0.90 \pm 0.05$ and $g \sim 0.37 \pm 0.15$ provide best match with data. Subsequently, we computed the ω_0 and g resulting from different size distributions, taking into account the complex refractive indices of ammonium hydrosulfide (NH_4SH) by Howett et al. [2007] and Ferraro et al. [1980]. Only the former data set is marginally consistent with JIRAM observations. Similarly, ammonia and hydrazine barely reproduce the experimental data. Tholin, although not usually considered a realistic component for Jupiter's aerosols, provides a better match for particle radii between 0.7 and 1 μm, both as a pure material as well as a thick coating over NH_4SH cores. Notably, this radius range is consistent with the mean radius of aerosols as estimated by Ragent et al. [1998] on the basis of Galileo entry probe data. Comparison with literature suggests that similar results can be achieved by a large variety of contaminants bearing C–N bounds.

Key words: techniques: photometric – planets and satellites: atmospheres – planets and satellites: individual: Jupiter.

1 INTRODUCTION

The infrared emission emerging from Jupiter's atmosphere at wavelengths around 5 μm has been measured both by ground-based instruments (e.g. Fletcher et al., 2016; Giles et al., 2016; Orton et al., 2017) as well as space-borne ones (Carlson et al., 1993; Roos-Serote et al., 1998, 1999; Giles et al., 2015). The brightness at 5 μm is highly time-variable, as shown by Fletcher et al. (2017) and Antuñano et al. (2018). An extensive data set, covering all latitudes, has been produced since 2016 by the Jupiter InfraRed Auroral Mapper (JIRAM) onboard the Juno spacecraft (see Adriani et al., 2014 for an instrument description and Adriani et al., 2018; Grassi et al., 2018, 2020 for selected results).

Arguably, the most remarkable feature of these observations is the strong radiance contrast between different regions, exceeding a factor of 100 at low and intermediate latitudes (50°S–40°N), with marked latitudinal trends (e.g. fig. 4b in Grassi et al., 2020). Most latitudes (especially those associated with bright 'zones' in the visible spectral range) display low-infrared emission, with equivalent brightness temperatures down to 170 K. Globally averaged equilibrium thermodynamic models (Atreya et al., 1999) expect the occurrence of at least three distinct cloud decks composed of water, ammonium hydrosulfide, and ammonia, from bottom to top. Optically thick clouds prevent most of the thermal radiation from deeper (warmer) levels from reaching the observer, and the measured signal essentially originates from the thermal emission of the atmosphere at the cloud tops. However, some subtleties should be taken into account. The optical thickness of the NH_3 ice cloud should be low enough to allow the emergence of some radiation from warmer regions at lower

★ E-mail: davide.grassi@inaf.it

altitudes, at least in the equatorial region (Drossart et al., 1998). Similarly, Irwin et al. (2001) demonstrated that variations in the 5 μm signal are correlated with opacity between 1 and 2 bars (the expected location of ammonium hydrosulfide clouds), rather than the thickness of the higher ammonia cloud. The brightness temperatures observed in low-emission regions are therefore consistent with a relatively thin upper cloud of ammonia located above an optically thick ammonium hydrosulfide cloud deck.

Other latitudes (notably those associated with dark 'belts' in the visible spectral range) exhibit higher infrared emission, with brightness temperatures exceeding 260 K. Under these conditions, the observer records photons thermally emitted at pressures of a few bars, with H_2 collision-induced absorption being the primary source of opacity at these wavelengths (Sromovsky & Fry, 2018). These photons experience only minor absorption from the thin cloud layers found in these regions.

At low latitudes, the higher infrared signal is observed in the so-called 'Hotspots,' which are large bright areas elongated in longitude (typically spanning a few thousand kilometres) found between the Equatorial Zone and the North Equatorial Belt (NEB). These areas are associated, in the visible spectral range, with grey 'festoons,' bluish 'dark projections' and 'dark formations' (see Rogers 1995 for an historical review and Choi et al., 2013). The low-cloud opacity of these areas was anticipated from ground-based data (Terrile & Westphal, 1977) before being confirmed by direct on-site measurements by the Galileo entry probe (GEP) (Ragent et al., 1998). There is consensus around the interpretation of these features as the result of trapped Rossby waves (Ortiz et al., 1998; Hueso et al., 1999; Showman and Dowling, 2000; Friedson 2005; Arregi et al., 2006). Several studies (Irwin et al., 1998; Roos-Serote et al., 1998; Nixon et al., 2001) investigated the Hotspots using spectra at wavelengths around 5 μm acquired by the near-infrared mapping spectrometer onboard the Galileo mission. More recently, we presented two studies (Grassi et al., 2017a, 2020) based on JIRAM spectral data, detailing the atmospheric composition within the Hotspots. Properties of Hotspots from thermal infrared and microwave data are discussed in Fletcher et al. (2020), along with their association with visible dark formations.

Our previous investigations were, however, based on a very simplified model for properties of residual aerosols over these features. Physical conditions in one Hotspot have been measured *in situ* by the GEP during its descent on 1995 December 7: the probe entered at 6.5°N 4.9°W, at the southern rim of a 5 μm Hotspot (Orton et al., 1998). The main aerosol layer encountered by the probe extended approximately between +7 and −8 km around the reference 1-bar isobaric surface, with a mean radius of particles between 0.8 and 1.1 μm (Ragent et al., 1998). While these observations provide the only direct measurements of the aerosol characteristics, it is not apparent whether they can be generalized to all Hotspots, especially considering that the Galileo probe entered one of the largest and long-lived Hotspots on Jupiter.

In this work, we discuss the observations of two Jupiter's Hotspots at 4.7 μm performed by JIRAM during the 12th Juno perijove passage on 2018 April 1. In this passage, JIRAM made repeated observations of the same large area of the NEB (including Hotspots) at a variety of emission angles ε. The variations of observed signal along ε (the so-called 'limb darkening') are used to constrain the scattering properties of aerosols (namely, the single scattering albedo ω_0 and asymmetry parameter g) and, indirectly, the size distribution. Several factors combine to make the Hotspots ideal targets for this type of analysis: (1) they are believed to have the simplest cloud structure that can be found over the disc of Jupiter, with essentially one relatively thin layer of aerosol (West et al., 2004); (2) their intrinsically strong infrared signal reduces the impact of possible residual calibration artefacts on our analysis; (3) their large spatial extent and smooth spatial variations minimize the ambiguities related to variable spatial resolution between different images.

2 DATA SET

The JIRAM instrument includes a spectrometer and two imaging channels operating in different spectral regions. In this paper, we will focus our attention solely on one of these channels (the so called *M*-filter), where images are acquired by integrating the incoming radiance over the 4.54–5.03 μm range. Images have a size of 432 × 128 pixels. All image pixels are acquired simultaneously, i.e.: the bidimensional image is formed directly on the focal plane and not by the stacking of consecutive lines in a push-broom scan. The field of view of individual pixels is about 240 μrad (Adriani et al., 2014). The random noise in calibrated *M*-filter images is by far dominated by shot noise. Data included in this analysis have an signal-to-noise ratio (SNR) between 20 and 80.

Juno is a spin-stabilized spacecraft and JIRAM acquires one image every Juno spacecraft rotation (2 rpm). JIRAM pointing has only one degree of freedom, and the pointing can be set only along the maximum circle orthogonal to the spin axis. Notably, such an arrangement allows JIRAM to compensate for Juno rotation during exposure. Acquisition of images often (but not necessarily always) occurs in sequences, i.e.: a set of consecutive images where the initial pointing angle is progressively increased (or decreased) in order to achieve, as far as possible, a continuous spatial coverage (i.e. a mosaic). Few examples of mosaics derived from such sequences are presented in Fig. 1.

During the 12th Juno perijove passage on 2018 April 1, JIRAM acquired a set of more than 210 individual images (arranged in 16 sequences) over Jupiter's equatorial region, within a time span of 3.5 h. The pixel resolution in the range from 5°N to 10°N varies between 395 and 83 km at the reference 1-bar level because of the high eccentricity of Juno's orbit. The same data have emission angles between 30° and 70°.

Table 1 lists the initial and final image that define each sequence selected for this study. The original calibrated data (Adriani et al., 2019) can be found at this Planetary Data System URL: https://atmos.nmsu.edu/PDS/data/PDS4/juno_jiram_bundle/data_calibrated/orbit12/.

Geometric parameters of each image (geographic locations of pixel corners and centres, solar zenith, emission and phase angles, and slant distance, etc.) are computed by means of the SPICE (Spacecraft, Planet, Instrument, C-matrix, Events) Toolkit (Acton, 1996, Acton et al., 2017) on the basis of the reconstructed kernel files available at https://naif.jpl.nasa.gov/pub/naif/JUNO/kernels/.

In this work, we consider JIRAM imaging data rather than JIRAM spectra, given the much larger number of pixels available. Moreover, only images acquired on the Jupiter's night side are included, to avoid the potential residual contribution to total signal from reflection of solar radiation.

3 METHODS

Our study used a series of spectral forward models to assess the trends of JIRAM signal I (as measured in *M*-filter images) versus emission angle ε, for different values of scattering parameters and cloud total opacity τ. As scattering parameters we consider (1) the single scattering albedo ω_0, i.e.: the ratio between the scattering cross-section and the total extinction cross-section of a particle; (2)
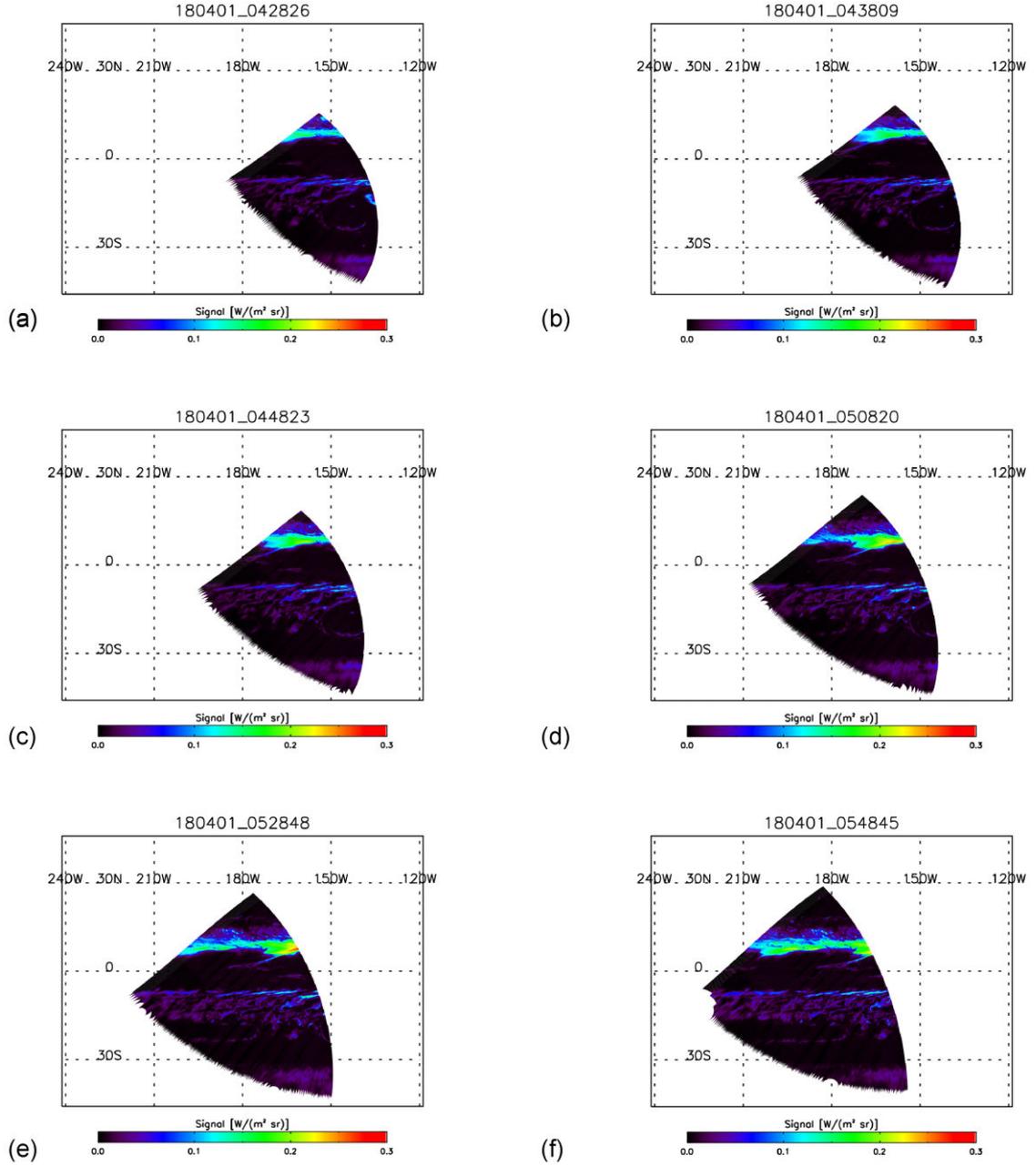
Figure 1. Mosaics of JIRAM *M*-band images acquired during the 12th Juno perijove passage. Each mosaic is derived from a single JIRAM sequence (see text for a definition). The title of each panel provides the central acquisition time according the scheme yymmdd_hhmmss. Note the progressive signal increase at (7°N, 162°W) in panels (a)–(e) caused by decreasing emission angles (see Table 1 for further details). Cylindrical projection is adopted.

the asymmetry parameter *g*, i.e.: the average value of the cosine of scattering angle. *g* = 0 implies isotropic scattering, while values close to 1 imply strong forward scattering.

We consider, for simplicity, the model of Hotspots described in Grassi et al. (2017b). Namely, this model assumes just one cloud, extended between −7 and +7 km (with respect to the 1 bar level) and the simplified representation of the gas mixing ratios profiles described in Irwin et al. (1998). Mixing ratios assumed for minor gases are the averages values observed in Hotspots, as presented in Grassi et al. (2020).

The forward code adopted to compute spectra (Ignatiev et al., 2005) has been modified to exploit the correlated-*k* tecnique (as described in Irwin et al., 2008). The multiple scattering is modelled

by means of DISORT algorithm (Stamnes et al., 1988), in the assumption of a Henyey–Greenstein phase function (developed in Legendre polynomials up to 64 streams). Resulting simulated spectra are multiplied by the *M*-filter response function to obtain theoretical *I* values. We fit the resulting simulated limb-darkening functions with a Minnaret's function, i.e.:

$$\mu \overset{\text{def}}{=\!=} \cos(\epsilon)$$
$$I(\mu) = I_0 \mu^k, \tag{1}$$

where I_0 and k are the free parameters of the fit. However, after initial tests, it became quickly evident that, even for a fixed pair of ω_0 and g values, (1) k – i.e.: the slope of the limb-darkening curve in the $\log(I) - \log(\mu)$ space – is not constant with μ, therefore making the

Table 1. JIRAM data considered in this study. Sequences are series of consecutive images acquired by the instrument, around the time given by sequence name according the scheme yymmdd_hhmmss. While sequence names were defined for the purposes of this work, the names of initial and last image corresponds to the nomenclature adopted in JIRAM data repository at NASA Planetary Data System (PDS). For each sequence, ranges of spatial resolution and emission angle for pixels in the latitude range 5N–10N are provided.

Sequence name *First image – last image*	Pixel resolution (min–max), km	Emission angle (min–max), degrees
180401_034801 *2018091T034404–2018091T035216*	395–281	70–62
180401_040758 *2018091T040401–2018091T041213*	331–201	67–52
180401_041812 *2018091T041415–2018091T042227*	285–180	64–48
180401_042826 *2018091T042429–2018091T043240*	298–163	66–45
180401_043809 *2018091T043412–2018091T044224*	314–151	68–42
180401_044823 *2018091T044426–2018091T045237*	261–139	64–39
180401_050820 *2018091T050423–2018091T051235*	292–124	68–34
180401_052848 *2018091T052450–2018091T053302*	252–112	66–32
180401_054845 *2018091T054447–2018091T055259*	222–103	64–30
180401_055859 *2018091T055501–2018091T060313*	230–99	66–31
180401_060913 *2018091T060515–2018091T061327*	170–96	59–31
180401_062909 *2018091T062512–2018091T063324*	126–91	51–33
180401_064937 *2018091T064540–2018091T065351*	107–87	48–37
180401_070934 *2018091T070536–2018091T071348*	102–84	50–41
180401_071948 *2018091T071550–2018091T072402*	105–83	53–44
180401_073001 *2018091T072604–2018091T072808*	110–83	57–46
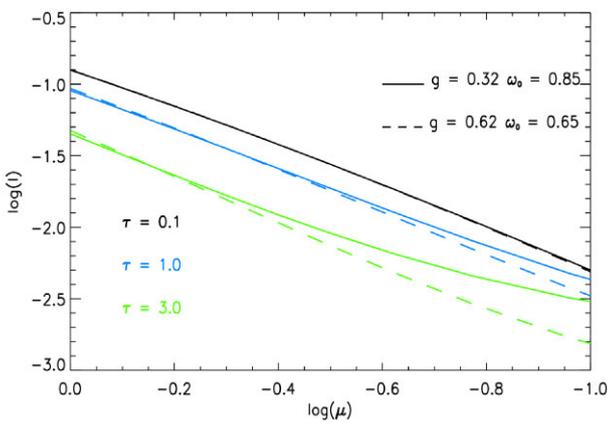
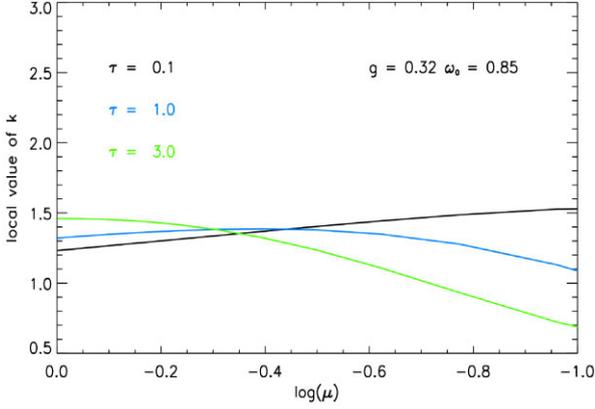**Figure 2.** Examples of theoretical limb-darkening functions for typical Hotspot conditions, for different cloud opacities τ. μ is the cosine of emission angle ε. Note that both axes are in logarithmic form, to highlight deviations from the Minnaret's formulation (see text).

upon opacity requires to include explicitly τ in whatever empirical function adopted to model the data, even when considering more sophisticated functions of μ and ε than Minnaret's one. Therefore, the inference of ω_0 and g from the limb-darkening trend *in a specific location* is necessarily limited by the ambiguity of the τ value to be assumed.

The method presented below circumvents this issue on the basis of several assumptions. First, we *assume* that ω_0 and g retain the same values over areas with different opacities inside the Hotspot. Then, we exploit the monotonic decrease of signal with increasing τ *at a fixed emission angle* for a given (ω_0, g) pair[1]. In the *further assumption* that observed signal variations are dominated by variations of τ – rather than by variations in composition, in vertical temperature profile or in cloud structure – the monotonic trend implies that the signal *at a given reference emission angle I_{ref}* – as inferred from the *observed* trend of I versus ε in a specific location – can be adopted as an effective proxy for τ there, in comparison with nearby areas. Potentially, this implies that repeated JIRAM observations of

Minnaret' function inadequate for our purposes, and, more important, (2) the k parameter at a fixed μ varies substantially with the optical depth τ (Figs 2 and 3). Notably, the dependency of limb darkening

---

[1]This holds true as long as clouds are located in a region of the atmosphere where temperature decreases with altitude, as is the case on Jupiter, where clouds are found well below the tropopause.

Figure 3. Examples of k values for Minnaret functions modelling theoretical limb darkening in typical Hotspot conditions. The parameter depends both on μ as well as on τ.

the same area at different emission angles allow us to sample the function $I = f_o(I_{ref}, \varepsilon)$ that, in turn, derives from a function $I = f_t(\tau, \varepsilon)$. The theoretical shape of f_o can be computed for any given pair of ω_0 and g values from simulated observations and compared directly with the observed shape.

In this preliminary phase of the study, a quick data inspection made clear the difficulties related to the study of more opaque regions, where the JIRAM signal becomes extremely low and it can be affected considerably by residual calibration artefacts (such as imperfect removal of thermal background). Moreover, Braude et al.

(2020) demonstrated that in regions of very high-opacity (notably, the adjacent Equatorial Zone) the simplistic Hotspot model of a single, thin, cloud is no longer appropriate and multiple cloud layers must be included.

In practical terms, the data analysis proceeds along the following steps:

(i) Each image in each of the sequences listed in Table 1 is mapped on the plane according to an azimuthal projection centred at $0°$N, $180°$W. The projection is performed for each of the four corners that define the istantaneous field-of-view (IFOV) of each individual JIRAM pixel. Before the projection, the longitude of each corner needs to be compensated for zonal motions occurring during the 3.5 h acquisition period. This is done by considering the wind profile by Porco et al. (2003) and adjusting each longitude to the same common time (06.30 UT 2018 April 1). Choi et al., (2013) pointed out the slight difference in speed between the NEB jetstreams ($\sim$114 m s^{-1}) and the dark formations associated to Hotspots ($\sim$103 m s^{-1}). Direct tests have shown that this difference in speed has no impact on our final estimates of ω_0 and g, nor on their corresponding uncertainties.

(ii) Over the projection plane considered above, we define a uniform, orthogonal sampling grid. The step of the grid is equal to 183 km at $0°$N, $180°$W. This grid defines the pixels for the resampled images produced at the next step (step 3).

(iv) For each projected image defined at step 1, we produce a resampled version over the grid defined at step 2. Each pixel of the original images contributes to the value of a pixel on the resampled image with a weight proportional to its spatial overlap. This step is required to compare different JIRAM images consistently. The
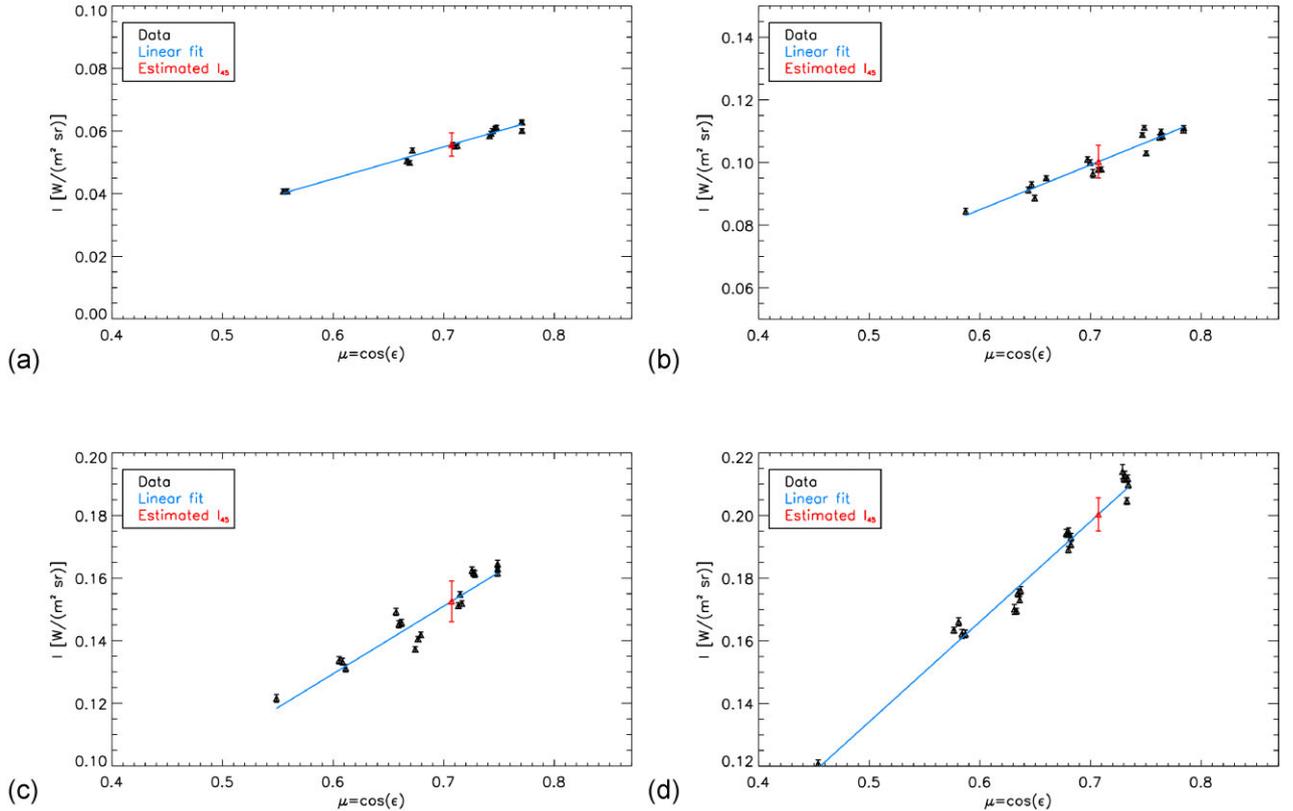
Figure 4. JIRAM data from a given location acquired at different emission angles are used to infer, by interpolation of a linear fit, the value at the reference emission angle of $45°$. Panels (a)–(d) present four examples at different absolute signal levels.
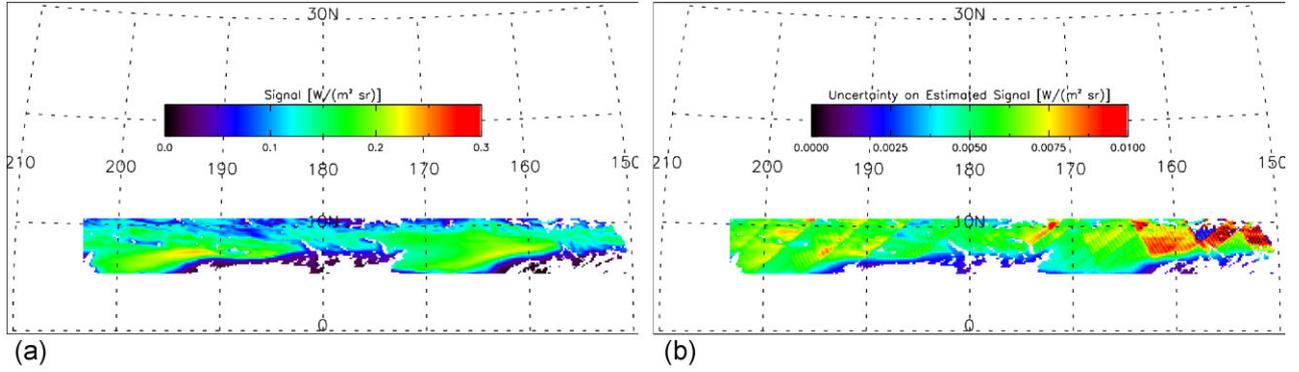
Figure 5. Estimated signal at $\varepsilon = 45°$ for the Hotspot region considered in this study (panel a) and corresponding uncertainties (panel b). Note the different colour scales of the two panels. *Two* distinct spatially adjacent Hotspots are covered by our data, being the one on the right (7°N, 162°W) the same shown in Fig. 1, panels (a)–(e), and the one on the left (7°N, 192°W) the same shown in Fig. 1, panels (e)–(f). Gaps in coverage are caused mostly by poor interpolation quality, often related to low signal.
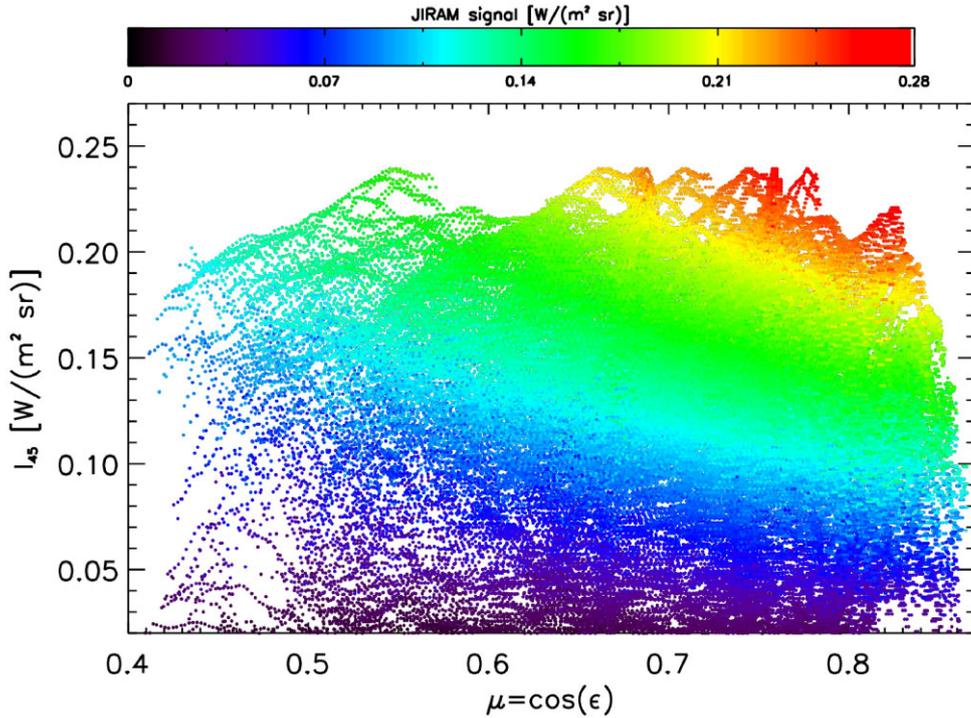

Figure 6. Experimental sampling of the surface $I = f_o(I_{45}, \mu)$, as derived from JIRAM observations. Individual points represent individual triplets, as described in the text.

value of the emission angle at the centre of each original pixel is also resampled in an analogous manner. Eventually, in each pixel of resampled images (now made spatially consistent with each other), we achieve a pair of values (signal I, emission angle ε) from each original image covering the area. *Hereafter, the term pixel will refer always to the resampled image.*

(v) These pairs allow one to estimate, by interpolation on their linear fit, the limb-darkening function for each pixel. Notably, this interpolation is performed for the *sole* purpose of estimating the radiance expected – for each pixel – at the reference emission angle of $\varepsilon = 45°$ (I_{45} hereafter) rather than to find a complete limb-darkening function such as those presented in Fig. 2. To reduce interpolation errors, the analysis is performed only for pixels where at least six pairs are available and the range of emission angles in JIRAM data encompasses the reference emission angle of 45° (i.e.: extrapolation

is not allowed). Given the spread in original JIRAM data and the limited range of ε, interpolation is performed assuming a linear fit, separately for each pixel (see examples in Fig. 4). Results of the fit are accepted (and the derived I_{45} included in the subsequent analysis) once the resulting intercept and slope have a value at least 10 times greater than corresponding uncertainties, as estimated from measurements errors and data spread. Eventually, uncertainties on linear fit parameters allow one to compute the uncertainty on the I_{45} estimated for each pixel. These latter uncertainties have a mean value of 0.006 W m^{-2} sr^{-1}, to be compared against a mean signal of 0.15 W m^{-2} sr^{-1}. Fig. 5 presents the I_{45} map derived in this analysis and corresponding uncertainties. Fig. 5(b) shows that uncertainties on I_{45} estimates are dominated by the spread of JIRAM data from different sequences – more evident in overlap regions – rather than by the uncertainty of signal in individual JIRAM images. This spread
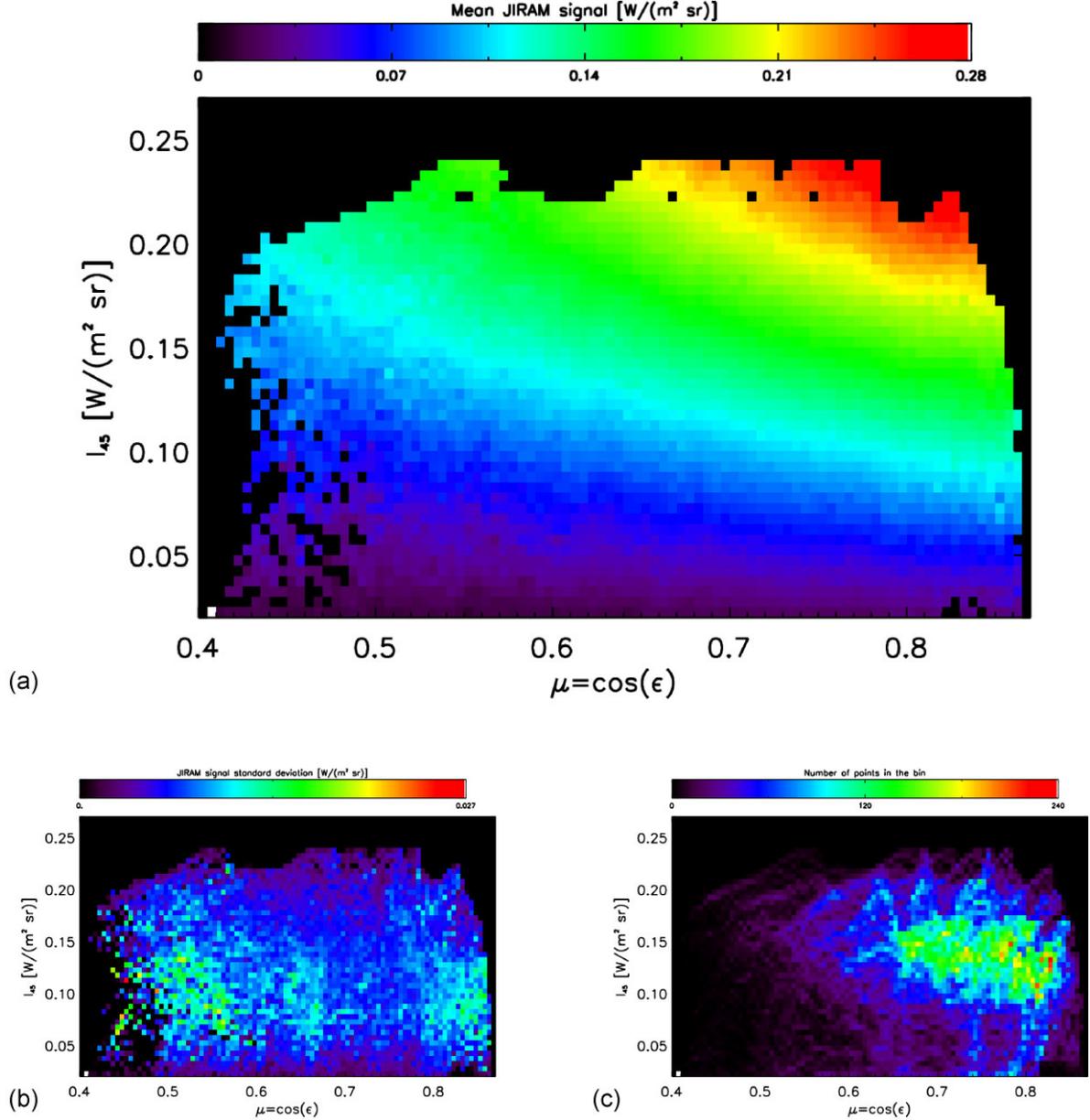
Figure 7. Data points from Fig. 6, once binned in the $(I_{45}, \mu = \cos(\varepsilon))$ space. Bins have widths of $0.005\,\mathrm{W\,m^{-2}\,sr^{-1}}$ and 0.005 (dimensionless) in the two directions. (a) Mean value of JIRAM signal (I) inside each bin. (b) Standard deviation of I inside each bin (note the different scale with respect to panel a). (c) Number of data points (triplets) inside each bin.

is due to residual calibration artefacts, most likely to be attributed to minor drifts in the instrument's temperature and amplifiers gains. The value of $\varepsilon = 45°$ is chosen as intermediate for the range of JIRAM observations (see Table 1).

(vi) At this step of the analysis, for each pixel, the original set of pairs derived in step 3 become a set of triplets (I, I_{45}, ε), I_{45} being identical for every triplet from the same pixel. These triplets can be seen as direct samples (z, x, y) of the $z = f_o(x, y)$ surface (i.e.: the $I = f_o(I_{ref}, \varepsilon)$ function described above) and represent the final experimental constraint offered by JIRAM data to be considered for comparison against theoretical simulations. The triplets considered in this study are presented in Fig. 6. Notably, the study excludes all the pixels where $I_{45} < 0.02\,\mathrm{W\,m^{-2}\,sr^{-1}}$, to reduce the possible effect of calibration artifacts, as discussed above. The overall distribution of the original pairs (I, ε) as derived in step 3 can also be inferred

from Fig. 6, as the distribution of points in the horizontal (ε) and out-of-the-page (I, colour-encoded) directions. To better clarify the experimental trends from JIRAM data, points in Fig. 6 were binned in the $(I_{45}, \mu = \cos(\varepsilon))$ space; mean and standard deviation of I inside each bin are presented in Fig. 7.

Considering now the theoretical simulations:

(i) A set of simulated JIRAM measurements is computed for each possible combination of the following inputs. ε: from 32.5° to 62.5° (with steps of 5°), $\tau = [0.01, 0.031, 0.1, 0.31, 1., 3.1, 10.]$, $\omega_0 = [0.75, 0.8, 0.85, 0.9, 0.95]$, $g = [0.22, 0.27, 0.32, 0.37, 0.42, 0.47, 0.52, 0.57, 0.62]$. Spectra are computed considering the same model and the same methods described for the preliminary simulations discussed at the beginning of this section, then multiplied by the
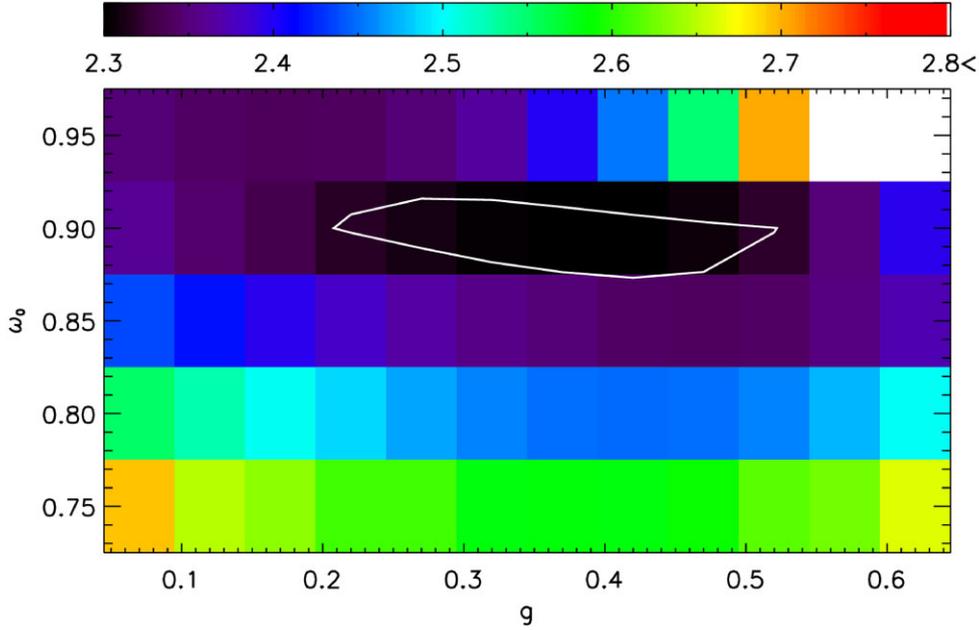
Figure 8. The dimensionless cost function C – measuring the discrepancy between the observed and theoretical f_o surfaces (see text for definition) – for different values of ω_0 and g. The white level curve indicates the 3σ uncertainty in the determination of minimum.

M-filter response function to estimate the JIRAM measurements $I(\varepsilon, \tau, \omega_0, g)$.

(ii) For each possible fixed pair of (ω_0, g) considered in simulations – and separately for each possible value of opacity τ – we interpolate the trend of signal I versus ε to estimate signal at the reference emission angle of $\varepsilon = 45°$.

(iii) For the given pair of (ω_0, g), each simulation now provides a triplet (I, I_{45}, ε), being I_{45} the same for every simulation with the same τ. The triplets for all τ are used to perform a polynomial fit of the $f_{o, \text{simul}}$ surface pertinent for the current pair of ω_0 and g.

For each pair of (ω_0, g), the parameters of the polynomial fit allow one to compute the value of f_{simul} at the (I_{45}, ε) positions of observed triplets described at point 5 of data analysis above, and to compute the total deviation against data as the sum of discrepancies over the entire population of experimental triplets. This ensures that the comparison is indeed performed in regions of f_0 actually covered by data. More explicitly, being: j an index to label individual triplets, $(I_{45}, \varepsilon)_j$ the I_{45} value and emission angle, respectively, for the j-th triplet, $f_{o,j}$ the observed signal I for the j-th triplet and $f_{\text{simul}}(I_{45}, \varepsilon)_j$ the simulated signal at the $(I_{45}, \varepsilon)_j$ position for a given (ω_0, g) pair, we can compute

$$C(\omega_0, g) = \sum_{j=1}^{N} \frac{\left[f_{\text{simul}}(I_{45}, \varepsilon)_j - f_{O,j} \right]^2}{S_j^2} / N, \qquad (2)$$

where S_j is an effective value of data spread in (I_{45}, ε) position of the j-th triplet, as estimated from Fig 7(b), and $N = 133\,653$ the total number of triplets considered.

This dimensionless quantity represents the cost function C to be minimized by varying (ω_0, g).

4 RESULTS

Fig. 8 presents the value of cost function C in the ω_0–g space. The lowest C value implies the best agreement with data. Despite the coarse sampling of ω_0–g space by our simulations (made necessary

by the high-computation times required by DISORT usage), a minimum is observed for $\omega_0 = 0.90$ and $g = 0.37$. In order to assess more directly the quality of the fit, it is useful to compare the trend of f_{simul} in the assumption of $\omega_0 = 0.90$ and $g = 0.37$ with the mean experimental JIRAM values (Fig. 7a). Fig. 9(a) presents this $f_{\text{simul}}(I_{45}, \varepsilon)$ over the same region of I_{45}–ε space sampled by JIRAM data, as well as its difference with respect to Fig. 7(a). The difference between theoretical and experimental surfaces (Fig. 9b) is, in general, well within the spread of experimental data as given in Fig. 7(b) (see Fig. 9(c) for the ratio between these quantities), especially in the regions better covered by experimental data (compare Fig. 9c and 7c).

Given the large number of steps in the analysis, it is difficult to perform a rigorous computation of the uncertainties on our ω_0 and g estimate.

To perform at least a rough assessment, we evaluated the variations of C associated with random fluctuations according to a simple bootstrap scheme. First, we computed the uncertainties σ_z associated with the I value of each triplet: this was done considering the uncertainties on the original JIRAM measurements and propagating them through the averaging process implicit in spatial resampling. Then, for each value of ω_0 and g, we performed one thousand trials t_i, by adding random fluctuations to the I value in each triplet (with zero mean and standard deviation equal to the specific σ_z pertinent to that triplet). At the same time, we also introduced random fluctuations on the I_{45} values of each triplet. These random fluctuations are statistically independent from those introduced on I and have standard deviations equal to the uncertainties on I_{45}, as estimated from the fit procedure described in previous Section 3, step 4. Finally, we recomputed the corresponding value of $C(\omega_0, g, t_i)$. The standard deviation of this 1000-element population (with elements from different t_i) can be seen as an effective uncertainty on the C values presented in Fig. 8. The level curve presented there corresponds to the minimum of C plus three times its uncertainty. Our estimate can therefore be better described as $\omega_0 = 0.90 \pm 0.05$ and $g = 0.37 \pm 0.15$. These values can be compared against
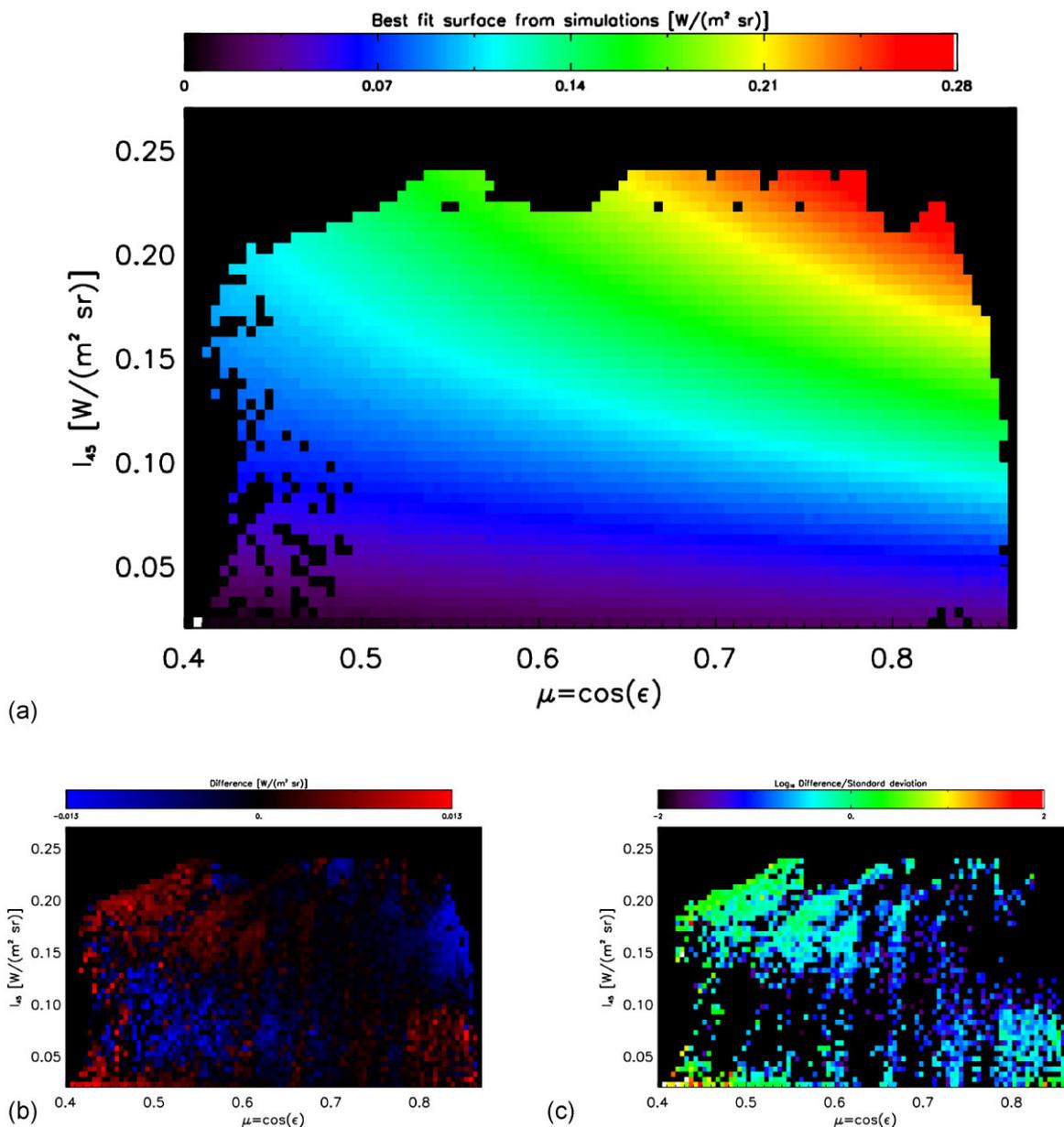
Figure 9. (a) Simulated $I = f_{simul}(I_{45}, \varepsilon)$ for $\omega_0 = 0.90$ and $g = 0.37$, best-fitting values inferred from Fig. 8. (b) Difference between experimental data and the best-fitting surface (i.e.: between Fig. 7a and Fig. 9a). (c) Ratio between fit discrepancies (Fig. 9a) and spread of experimental data (Fig. 7b).

the estimates of Giles et al. (2015) in the same spectral region, who adopted $\omega_0 = 0.9$ and $g = 0.7$ in their analysis of Cassini VIMS data. However, their work is based on data acquired 'in the equatorial region of the planet ($-2.5°$ to $2.5°$)' and therefore in very different physical conditions that those of the Hotspots considered here.

In order to address the dependency of our results on the simulation assumptions, we repeated the fit procedure for the search of g and ω_0 best values, considering the following variations.

(1) The entire set of simulated spectra computations was repeated by shifting, for all cases, the residual cloud from the original altitude $[-7;+7]$ km down to $[-14,-7]$ km. While the Galileo entry probe nephelometer measurements are indeed consistent with our original assumption (see summary table 5.1 in West et al., 2004 with the main cloud located between 0.75 and 1.3 bars), lower clouds in Hotspots between 1.3 and 1.6 bars (altitudes between -7 and -14 km) are

predicted by the theoretical model of Hueso et al. (1999). Lower clouds lead to g and ω_0 values of 0.42 and 0.90, respectively, consistent – within uncertainties – with our estimate at the original cloud altitude.

The entire set of simulated spectra computations was repeated by increasing, for all cases, the air temperatures of $+14$ K at all pressure levels. While the original $T(p)$ profile is the same measured by the Galileo entry probe (Ragent et al., 1998), the theoretical model by Hueso et al. (1999) predicts temperature deficiencies in the Hotspots up to 6 K with respect to the surrounding environment (Fig. 3, panel E there). Despite air temperatures highly exceeding expected variations, the resulting g and ω_0 values (0.42 and 0.85, respectively) are again consistent – within uncertainties – with our estimate from original assumptions.

The entire set of simulated spectra computations was repeated by expanding, for all cases, the residual cloud from the original
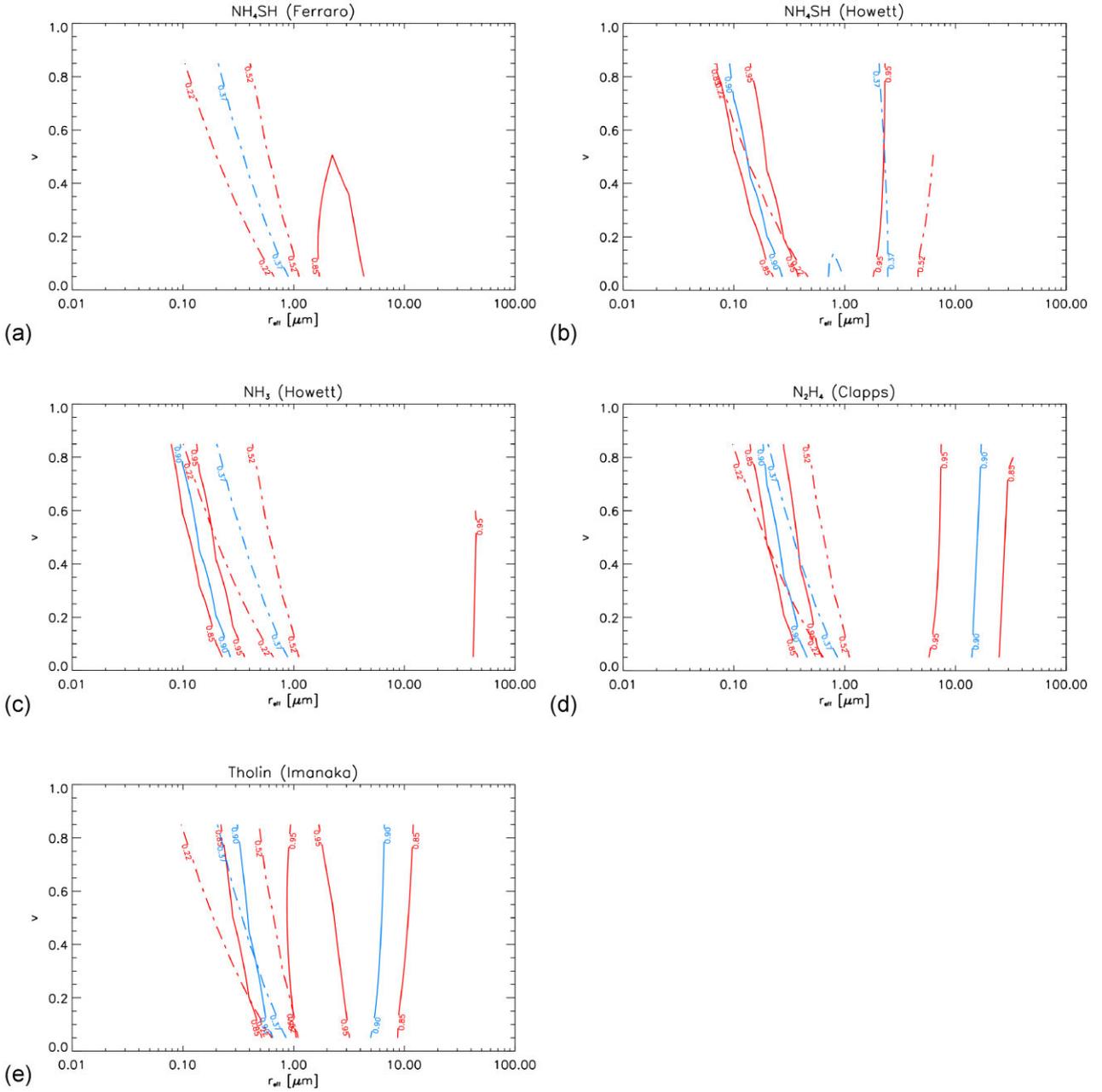
Figure 10. Contour lines for ω_0 (solid curves) and g (dashed curves) in the r_{eff}–variance space. Blue curves give the values estimated from JIRAM data, red curves the acceptance region bounded by corresponding uncertainties as estimated from Fig. 8. (a) NH$_4$SH, with complex refractive indices from Ferraro et al.. (b) NH$_4$SH, from Howett et al.. (c) NH$_3$, from Howett et al.. (d) N$_2$H$_4$, from Clapp and Miller. (e) tholin type 2 from Imanaka et al..

extension $[-7; +7]$ km to $[-14, +7]$ km. Broader clouds lead to g and ω_0 values of 0.32 and 0.90 respectively, consistent – within uncertainties – with our estimate for the original extension assumption.

With a further assumption on cloud composition, the scattering parameters ω_0 and g derived from our analysis can provide constraints on the size distribution of cloud particles. Ammonium hydrosulfide (NH$_4$SH) ice remains the most likely candidate as the *main* component of residual clouds over Hotspots (Atreya et al., 1999), although our analysis of the solar-dominated short-wavelength spectral region presented in Grassi et al. (2021) suggests that contamination from other components may be important in other low-latitude regions of the planet. The coating of clouds with

complex haze produced photochemically was originally proposed and extensively discussed by Atreya et al. (2005). Complex refractive indices of solid ammonium hydrosulfide have been inferred from experimental transmissivity measurements described in the two independent studies by Ferraro et al., (1980) and Howett et al., (2007). However, Ferraro et al., (1980) did not publish any final (n, k) table and the derived refractive indices have been circulated only informally in the science community since then. For the purposes of this study, we considered $n = 1.38$ and $k = 0.020$ as the Ferraro et al. (1980) effective values for the JIRAM M-filter. With the simplifying assumption of spherical particles (indeed, a rather strong assumption for ice particles) and for a given set of refractive indices, Mie theory allows us to compute the expected (ω_0, g) for each possible pair of
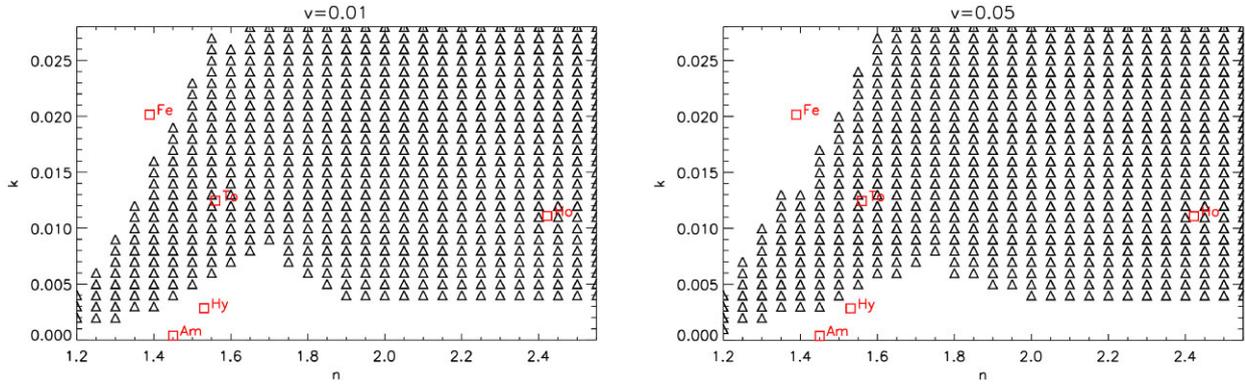
Figure 11. The plots display with black triangles the regions of the *n*–*k* space (real and imaginary parts of refractive index, respectively) that satisfy the two constraints $0.85 < \omega_0 < 0.95$ and $0.22 < g < 0.52$ for any $r_{\rm eff}$ in the range 0.3–3.0 μm. Red squares provide, for reference, the refractive indices at 4.8 μm for different putative components of Jupiter's clouds. *Hy*: N_2H_4, from Clapp and Miller, *Am*: NH_3, from Howett et al., *Fe*: NH_4SH, from Ferraro et al., *Ho*: NH_4SH, from Howett et al., *To*: tholin type 2 from Imanaka et al.. (a) For a size distribution variance of 0.01. (b) For a size distribution variance of 0.05.

parameters effective radius ($r_{\rm eff}$) and variance (v) describing a size distribution.

Fig. 10 presents the results of these Mie computations. Namely, we show the regions in the $r_{\rm eff}$–v space centred around the contour lines corresponding to the ω_0 and g values inferred from JIRAM and bounded by their respective uncertainties. We define these regions as acceptance regions. Overlaps in acceptance regions of ω_0 and g shall be considered consistent with data. The Ferraro et al. (1980) set (Fig. 10a) is not consistent with JIRAM-derived estimates, mostly because of the difficulty in producing the required high ω_0 with high values of k (i.e.: absorption coefficients). The simulations based on Howett et al. (2007) data (Fig. 10b) produce the required combination of ω_0 and g in two distinct regions of $r_{\rm eff}$–v space. The first region starts at $v = 0.2$ and $r_{\rm eff} = 0.3$ μm and extend to smaller radii and higher variances. The second region develops between 2 and 4 μm in a large range of variances. Notably, in neither of the two areas we have a crossing of the curve levels corresponding to $\omega_0 = 0.90$ and $g = 0.37$. *Pure* ammonia ice (as modelled by the refractive indices in Howett et al. (2007, Fig. 10c) produces a marginally consistent region, developing from $v = 0.6$ and $r_{\rm eff} = 0.2$ μm and extending to smaller radii and higher variances. More convincing agreement is provided by hydrazine (as given in Clapp and Miller 1996, Fig. 10d), where the consistent area starts at $v = 0.1$ and $r_{\rm eff} = 0.2$ μm. We also considered the tholin material (Imanaka et al., 2012) adopted in our previous paper Grassi et al. (2021), there chosen for its capability to reproduce the shape of the reflectance spectral maximum seen in JIRAM spectra at 2.74 μm. While this material cannot be considered as a realistic candidate for the main component of Jupiter clouds (tholin are simulants of the products of N_2–CH_4 photochemistry on Titan), it can none the less reproduce an external coating by a poorly characterized compound that includes N–H bounds responsible for the absorption band observed in Jupiter spectra around 3 μm (Sromovsky and Fry 2010). Fig. 10(e) presents the results of Mie computation for pure tholin. The overlap of acceptance regions for ω_0 and g is achieved for $0.4 < r_{\rm eff} < 1$ μm and a rather large range of v, including the very low values previously considered in literature (e.g.: 0.05 in Irwin et al. 1998). Notably, among pure materials, tholin is the only one capable to produce crossing of the curve levels corresponding to $\omega_0 = 0.90$ and $g = 0.37$, achieved for $v = 0.3$ and $r_{\rm eff} = 0.45$ μm.

For sake of completeness, we investigated the space $r_{\rm eff}$–n–k (being n, k the real and imaginary parts of the refractive index at 4.8 μm) to

determine which combinations are consistent with JIRAM data. The results are presented in Fig. 11. As previously observed, both NH_4SH (according Howett et al.) and tholin can produce consistent results, while other pure materials considered have imaginary components of refractive index either too low (hydrazine and ammonia) or too high (NH_4SH according Ferraro). From the panels on Fig. 10 we can also observe that the acceptance region where $0.85 < \omega_0 < 0.95$ moves consistently toward low $r_{\rm eff}$ while k decreases.

We also considered the case of coated particles, formed by a NH_4SH core (as modelled by Howett et al. 2007 indices) and an external coating (i.e.: an outer layer) formed by ammonia, hydrazine or tholin. The scattering properties of these spherical coated particles were computed by mean of the BART code (Quirantes, 2020). Results are shown in Fig. 12, where we considered relative core-to-particle radius ratios of 0.85 and 0.15. These two values are intended to represent cases dominated by the core or by the coating, respectively. The coated particles considered in our simulations seem not adequate to produce a significant improve of overlap regions once compared to pure materials. Coated particles dominated by the NH_4SH core (Fig. 12a–e) retain a first region consistent with JIRAM estimates for $2 < r_{\rm eff} < 3$ μm and second for $r_{\rm eff} < 0.4$ μm and high v (very small for ammonia, more pronounced for tholin). In no case, we observe a crossing of the curve levels corresponding to $\omega_0 = 0.90$ and $g = 0.37$. Particles dominated by coatings (Fig. 12b, d, f) largely reproduce the properties previously observed for the corresponding pure materials. Tholin coating provides the most convincing match with JIRAM-derived values of ω_0 and g, for radii between 0.7 and 1 μm. These values can be compared against the average particle radius of 0.8–1.1 μm reported by Ragent et al. (1998) for the residual cloud in Hotspots measured by the Galileo entry probe nephelometer.

5 DISCUSSION

The results presented in the previous section depends on a number of assumptions, most notably, on the hypothesis that brightness variations inferred from JIRAM data at the reference emission angle are mostly driven by variations in the optical thickness of clouds. Unfortunately, such an assumption cannot be circumvented with repeated observations of the same region, since such an observation does not – alone – address the dependence of limb-darkening function upon cloud opacity shown in Fig. 3. Longitudinal variations in
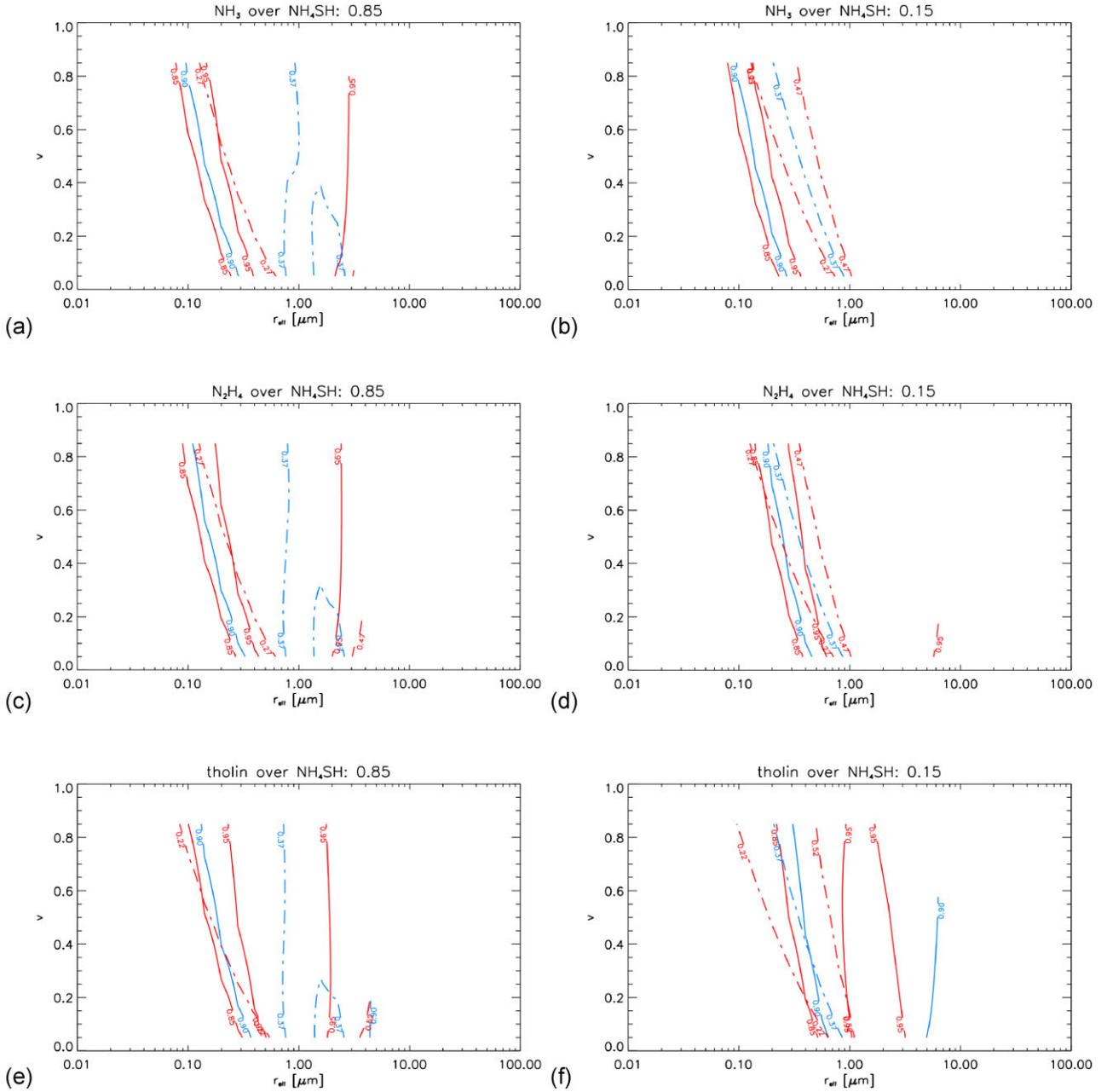
Figure 12. As Fig. 10, for coated particles formed by a NH$_4$SH core (Howett et al.) and different coatings. (a), (b) NH$_3$ coating. (c), (d) N$_2$H$_4$ coating. (e), (f) Tholin coating. 0.85 and 0.15 labels provide the core-to-particle radii ratio (0.85 large core, 0.15 small core).

the amounts of water vapour and ammonia inside Hotspots, such as those presented in Grassi et al. (2020; figs 7c and 8c there), and in Fletcher et al. (2020) are probably the main limit of our analysis.

JIRAM estimates are consistent – within uncertainties – either with NH$_4$SH-dominated particles with radii between 2 and 3 μm or, alternatively, with smaller particles (0.7–1 μm) dominated by contaminants (modelled by tholin). The latter scenario appears more convincing, given (a) the best correspondence with the JIRAM estimates and (b) the consistency with independent size measurements by Galileo entry probe.

We noticed also that the refractive indices of the organic samples produced by ion bombardment of ices (N$_2$:CH$_4$:CO) described in

Baratta et al. (2015) have a value of [1.6, 0.07], also consistent with JIRAM data, as demonstrated by Fig. 11. Both in the case of Imanaka et al. (2012) tholin as well as for the organic samples of Baratta et al. (2015), the value of k in the band of JIRAM images is substantially risen by a sharp absorption feature located at about 2180 cm^{-1} ($\sim$4.58 μm, see figs 3–6 in Imanaka et al. and fig. 11 in Baratta et al). The latter paper interprets this feature as caused by C$\equiv$N bounds in the sample. Furthermore, Carlson et al. (2016) describe the optical properties of a chromophore from photolyzed ammonia reacting with acetylene, to simulate the specific conditions of Jupiter atmosphere. Although these authors do not provide refractive indices values for the spectral range of our interest, they present an absorption spectrum of the material, with a clear sharp feature at 2056 cm^{-1} ($\sim$4.86 μm)

interpreted as due to diazo hydrocarbons (C=N=N). Therefore, it appears that intermediate k values ($\sim$0.01) along with low n values ($\sim$1.6) are common among the by-products of degradation of carbon- and nitrogen-bearing species.

Results from Braude et al ([2020], fig. 13d there) suggests a substantial increase of r_{eff} for the equatorial clouds considered by Giles et al. ([2015]). Both Figs [10] and [12] point toward a general increase of the asymmetry parameter g for increasing r_{eff}, and the discrepancy in the g estimates provided here and in Giles et al. ([2015]) can probably be reconciled considering the different particle sizes in the areas considered in the two studies. Notably, r_{eff} variations produce much less pronounced variations on ω_0, that is indeed consistent in the two studies.

The model of Hotspots presented by Friedson ([2005]) foresees that air parcles, flowing from west to east, descend from altitudes well above the 0.6 bar isosurface down to the 1.3-bar surface (base of residual cloud in our model) when they encounter the minimum of the Rossby wave (corresponding to brighter regions in the infrared), moving along the isolevels of potential temperature Θ (fig. 8 there). Substantial downdraft in the brightest regions of Hotspots was also expected in the model of Hueso et al. ([1999]). This scenario is consistent with the occurrence of substantial amounts of contaminants produced by the combination of hydrocarbon haze particles falling from Jupiter's stratosphere and hydrazine created by photodissociation of ammonia in the upper troposphere (Atreya et al. [2005]) at the location of residual clouds over Hotspots.

6 CONCLUSIONS

JIRAM M-filter images acquired over Jupiter's 5-$µ$m-bright Hotspots during the 12th Juno perijove passage have been analysed to constrain, through the study of limb darkening, the scattering properties of residual clouds. Our results point toward a relatively small particle size ($r_{eff} \sim 1.0\ µ$m) for these clouds and the occurrence of contaminants, possibly over the putative cores of ammonium hydrosulfide. The presence of contaminants is consistent with the downward air motions expected by theoretical models over brightest regions of Hotspots. Further theoretical work will be required to compare the typical lifetimes of NH_4SH cloud particles in Hotspots (where they are subject to periodic sublimation/condensation associated to the vertical air motions associated to the Rossby wave) against the times required to accumulate an amount of contaminants on their surface adequate to mask their optical properties.

These results allow a refinement of previous analysis of JIRAM spectra, with improved treatment of scattering by residual clouds in computation of theoretical spectra. The information content of limb-darkening measurements demonstrated by this study strongly support the inclusion joint spectral/limb-darkening measurements in the planning of instruments capable of acquiring extended spectral data sets at high-spatial resolution, notably MAJIS onboard the European Space Agency's JUICE mission.

DATA AVAILABILITY

The original calibrated data (Adriani et al., [2019]) used in this study can be found at this Planetary Data System URL: https://atmos.nmsu.edu/PDS/data/PDS4/juno_jiram_bundle/data_calibrated/orbit12/.

Geometric parameters of each image (geographic locations of pixel corners and centres, solar zenith, emission and phase angles, slant distance, etc.) were computed by means of the SPICE Toolkit (Acton, [1996], Acton et al., [2017]) on the basis of the reconstructed kernel files available at https://naif.jpl.nasa.gov/pub/naif/JUNO/kernels/.

REFERENCES

Acton C. H. et al., 2017, Planet. Space Sci., 150, 9
Acton C. H., 1996, Planet. Space Sci., 44, 65
Adriani A. et al., 2014, Space Sci. Rev., 213, 393
Adriani A. et al., 2018, Nature, 555, 216
Adriani A., Noschese R., Huber L., 2019, PDS Atmospheres, (ATM) Node, last accessed: 2024 August 21
Antuñano A. et al., 2018, Geophys. Res. Lett., 45, 987
Arregi J. et al., 2006, J. Geophys. Res. (Planets), 111, 9010
Atreya S. K. et al., 1999, Planet. Space Sci., 47, 1243
Atreya S. K. et al., 2005, Planet. Space Sci., 53, 498
Baratta G. A. et al., 2015, Planet. Space Sci., 118, 211
Braude A. S. et al., 2020, Icarus, 338, 113589
Carlson B. E. et al., 1993, J. Geophys. Res., 98, 5251
Carlson R. W. et al., 2016, Icarus, 274, 106
Choi D. et al., 2013, Icarus, 223, 832
Clapp M. L., Miller R. E., 1996, Icarus, 123, 396
Drossart P. et al., 1998, J. Geophys. Res., 103, 23043
Ferraro J. R. et al., 1980, Appl. Spectrosc., 34, 525
Fletcher L. N. et al., 2016, Icarus, 278, 128 .
Fletcher L. N. et al., 2017, Geophys. Res. Lett., 44, 7140 .
Fletcher L. N. et al., 2020, J. Geophys. Res. Planets, 125, e2020JE006399
Friedson A. J., 2005, Icarus, 177, 1
Giles R. S. et al., 2015, Icarus, 257, 457
Giles R. S. et al., 2016, Icarus, 289, 254
Grassi D. et al., 2017a, Geophys. Res. Lett., 44, 4615
Grassi D. et al., 2017b, J. Quant. Spectrosc. Radiat. Transfer, 202, 200
Grassi D. et al., 2018, J. Geophys. Res. (Planets), 123, 1511
Grassi D. et al., 2020, J. Geophys. Res. (Planets), 125, e2019JE006206
Grassi D. et al., 2021, MNRAS, 503, 4892
Howett C. J. A. et al., 2007, J. Opt. Soc. Am. B, 24, 126
Hueso R. et al., 1999, Planet. Space Sci., 47, 1263
Ignatiev N. I. et al., 2005, Planet. Space Sci., 53, 1035
Imanaka H. et al., 2012, Icaurs, 218, 247
Irwin P. G. J. et al., 1998, J. Geophys. Res., 103, 23001
Irwin P. G. J. et al., 2001, Icarus, 149, 397
Irwin P. G. J. et al., 2008, J. Quant. Spectrosc. Radiat. Transfer, 109, 1136
Nixon C. A. et al., 2001, Icarus, 150, 48
Ortiz J. L. et al., 1998, J. Geophys. Res., 103, 23051
Orton G. S. et al., 1998, J. Geophys. Res., 103, 22791

Orton G. S. et al., 2017, Geophys. Res. Lett., 44, 4607

Porco C. et al., 2003, Science, 299, 1541

Quirantes A., 2020, *BART Code Source File*. Retrieved at https://www.ugr.es/~aquiran/codigos.htm, last accessed: 2024 August 21

Ragent B. et al., 1998, J. Geophys. Res., 103, 22891

Rogers J. H., 1995, The Giant Planet Jupiter, Cambridge Univ. Press, Cambridge

Roos-Serote M. et al., 1998, J. Geophys. Res., 103, 23023

Roos-Serote M. et al., 1999, Icarus, 137, 315

Showman A. P., Dowling T. E., 2000, Science, 289, 1737

Sromovsky L. A., Fry P. M., 2010, Icarus, 210, 230

Sromovsky L. A., Fry P. M. 2018 Icarus, 307 347

Stamnes K. et al., 1988, Appl. Opt., 27, 2502

Terrile R. J., Westphal J. A., 1977, Icarus, 30, 274

West R. A., Baines K. H., Friedson A. J., Banfield D., Ragent B., Taylor F. W., 2004, in Bagenal F., Dowling T. E., McKinnon W. B., eds, Jupiter: The Planet, Satellites and Magnetosphere, Cambridge Planetary Science Series. Cambridge University Press, Cambridge, UK

This paper has been typeset from a TEX/LATEX file prepared by the author.